Controller design and implementation of six-degree-of-freedom magnetically levitated positioning system with high precision

H Yu and **W-J Kim***
Department of Mechanical Engineering, Texas A&M University, Texas, USA

Abstract: This paper presents the controller design and implementation of a high-precision six-degree-of-freedom (6-DOF) magnetically levitated (maglev) positioner. This high-precision positioning system consists of a novel concentrated-field magnet matrix and a triangular single moving part that carries three three-phase permanent-magnet planar-levitation-motor armatures. Since only a single levitated moving part, namely the platen, generates all required fine and coarse motions, this positioning system is reliable and potentially low-cost. The three planar levitation motors based on the Lorentz force law not only produce the vertical force to levitate the triangular platen but also control the platen's position and orientation in the horizontal plane. The main contribution of this paper is that all 6-DOF motions are solely controlled by magnetic forces without any other means to support the platen's weight against gravity, and the most suitable controller of the magnetic levitation system was designed and implemented. The platen can be regarded as a pure mass, and the spring and damping effects are neglected except for the vertical directions. Single-input single-output digital lead-lag controllers were designed and implemented on a digital signal processor. This 6-DOF fully magnetically levitated positioner has a total mass of 5.91 kg and exhibits a 120×120 mm maximum travel range. The position resolution of 20 nm and position noise of 10-nm root mean square are demonstrated. The positioner has sub-microradian angular resolution in about the x, y, and z-axes. A maximum velocity of 24.8 mm/s in y is achieved. This single-moving-part maglev positioner structure is highly suitable for semiconductor manufacturing applications such as wafer steppers. Several experimental motion profiles are presented to demonstrate the maglev stage's capability of accurately tracking any planar and three-dimensional paths.

Keywords: real-time digital control, magnetic levitation, nanoscale positioning, 6-DOF positioning, precision manufacturing

1 INTRODUCTION

The wafer steppers, surface profilometers, and scanned-probe microscopes used in modern nanoscale and microscale engineering applications require high-precision motion control. The use of wafer steppers in semiconductor manufacturing is a main target application of the work presented in this paper. The wafer stepper generates step-and-repeat motions and is a crucial piece of equipment in photolithography-based processes. In photolithography an optical source projects a deep-ultraviolet (light) beam through a photomask or reticle onto each die site on a wafer. The wafer stage is required to move the wafer in all six axes with a high resolution and accuracy and with a long multi-dimensional travel range, a high control bandwidth, and produce only minimal mechanical vibration. In this paper, a six-degree-of-freedom (6-DOF) high-precision magnifically levitated (maglev) positioner that could be used in a next-generation wafer stage is presented.

*Corresponding author: Department of Mechanical Engineering, Texas A&M University, College Station, Texas 77840, USA. email: wjkim@mengr.tamu.edu

Conventional precision positioners used in industry can be split into one of two types: the crossed axis or gantry types. A crossed axis positioner has the stages' axes on top of one another. The moving parts are usually controlled by stepper motors and ball screws. In order to reduce friction, some positioners employ air bearings despite their complicated design. Gantry-type positioners have a bridge-like frame, and the mover is controlled by two motors at the end of the bridge. This kind of positioner is used in scanners and plotters that do not require high positioning resolution. These traditional positioners suffer from significant drawbacks including not being able to inherently generate rotational motions. Although rotational motions could be produced by additional devices, the whole positioner's machine structure would be more complicated and bulkier since each axis of motion requires a dedicated actuator. As a result, the whole positioning system could exhibit significant dynamic coupling and be difficult to control. [1–7].

A permanent-magnet-matrix planar motor uses a number of permanent-magnet cubes instead of iron protrusions as in the base plate of a Sawyer motor [8]. This permanent-magnet matrix forms a stator in cross-stripe patterns. If the current flows in the windings attached to the bottom surface of the platen, a magnetic force is generated. Asakawa proposed the first permanent-magnet planar motor by orthogonally superimposing two conventional one-dimensional magnet arrays [9, 10]. The 6-DOF maglev positioner presented in this paper uses a superimposed Halbach magnet-matrix array. This structure, also called a synchronous permanent-magnet planar motor (SPMPM), has improved dynamics compared to the Sawyer motor and traditional permanent-magnet planar motors [11–15].

The Sawyer motor was commercialized by Northern Magnetics and Megamation. However, it suffers from the following drawbacks.

1. The two-phase full-step size has a coarseness of 250 µm, which can be possibly reduced by micro-stepping.
2. The Sawyer motor needs a tight air gap of less than 25 µm, so it requires an ultrafine surface finish of the motor surfaces.
3. Its position repeatability only measures 5 µm.
4. In addition to a large cogging force, the attractive force of one model is as high as 1800 N [16].

Megamation's x–y stage has been used in an IBM printed-circuit-board assembly line, and its accuracy specification is about 25 µm [17].

In Fig. 1(a), on the bottom surface of the single moving part, namely the platen, a two-dimensional superimposed concentrated-field double-axis magnet matrix is attached. A conceptual creation of the novel double-axis magnet matrix is a linear superimposition of two orthogonal Halbach magnet arrays [18]. The stator currents flow in orthogonally interwoven multi-phase x- and y-windings. The stator currents in the x- and y-windings generate an air gap magnetic field that travels in the x- and y-directions, respectively. Consequently, the x- and y-stator currents interact only with the corresponding x- and y-magnet-array component. An alternative positioner concept, shown in Fig. 1(b), carries the windings that energize the actuation system on the platen. Figure 2 demonstrates the working principle of this technology.

Figure 3 shows photographs of the high-precision 6-DOF maglev positioner. It consists of a single moving platen with three planar levitation motors and two stick mirrors, a base plate with a magnet matrix, three laser distance sensors, and three laser interferometers. This positioner uses three SPMPMs, that serve as actuators, to overcome the shortcomings of traditional planar motors [1, 2]. Its most significant advantage is that the single levitated moving part, namely the platen, can generate all 6-DOF fine and coarse motions. In addition, there are several additional advantages.

1. A mechanically non-contacting machine structure does not need a lubricant and does not produce wear particles. Therefore, it is can be used in clean-room environments.
2. Superimposing multiple linear motors to produce a single actuator reduces the footprint.
3. Compared to traditional positioners, the single moving frame can have high natural frequencies.
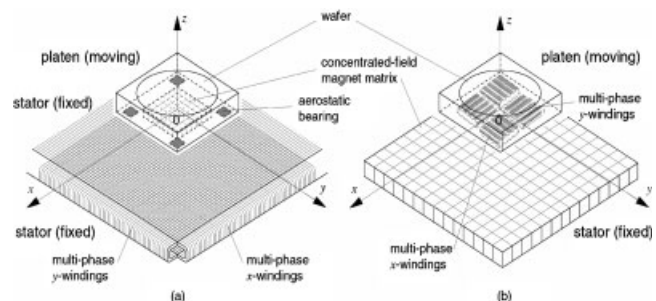
Fig. 1 Perspective views of integrated 6-DOF maglev positioner concepts: (a) moving-magnet-stationary-winding design, (b) moving-winding-stationary-magnet design
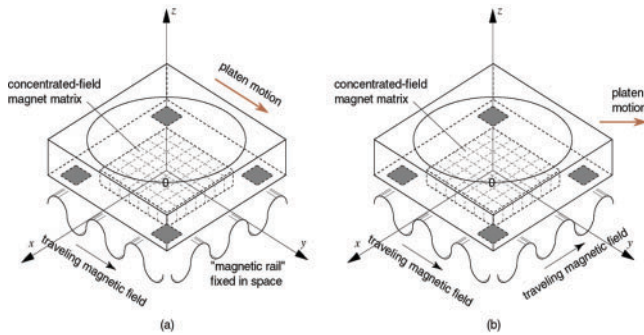
Fig. 2 Working principle of the positioning technology. For visualization purposes, the windings were replaced with the sinusoidal waves of the magnetic field generated by the multi-phase stator currents. (a) *y*-directional motion generation. The magnetic field generated by the *x*-windings is stationary (without commutation) and serves as a 'magnetic rail' so that the platen does not move in the *x*-direction. (b) Diagonal motion generation by controlling the phase currents in the *x*- and *y*-windings, independently

4. Its simple design eliminates complicated components, reduces manufacturing cost, and results in a high reliability [**19**, **20**].

This 6-DOF positioner has a 5.91 kg platen and exhibits a 120×120 mm experimental maximum planar travel range. The frame of the platen was made of Delrin with a mass density of 1.54 g/cm^3 in order to reduce its total mass. Its triangular structure was chosen for design simplicity. The superimposed concentrated-field double-axis magnet matrix serves as a stator. The dimension of the magnet matrix is $304.8 \times 304.8 \times 12.7$ mm. The high-precision stick mirrors (manufactured by Bond Optics) reflect the laser beams that are used to measure the platen's planar displacement and velocity using the three laser interferometers. The design and manufacture of this system is discussed in detail in [**20**].

2 INSTRUMENTATION

2.1 Control structure

Figure 4 is a schematic diagram of the control structure for the signal and data flows for the 6-DOF precision positioner. In an interrupt service routine, all data flows, such as position and velocity information, control outputs, and mutual interaction, are achieved. The Pentek 4284 digital signal processor (DSP) runs at a sampling frequency of 5 kHz.

2.2 Digital signal processor

The Pentek 4284 DSP board contains a TMS320C40 DSP produced by Texas Instruments that operates with a 50 million-floating-point-operations-per-second computational capability. This DSP board has a VMEbus as a controller. The laser-axis boards (Agilent 10897B) and the data-acquisition board send the real-time sensor data to the DSP board, and the DSP sends the output commands to the 12 bit digital-to-analogue converter (DAC) board (DATEL DVME622). Control outputs communicated to the DSP board flow to individual coils through a nine-channel power amplifier. With this 12 bit DAC board, the current quantization is $1.1348/2^{12}$ A. The force constant value (calculated using equation (4) that will be presented in section 3.2) is 20.3695 N/A. Therefore, the force quantization level is $20.3695 \times (1.1348/2^{12}) = 5.6433 \times 10^{-3}$ N.

2.3 Control software

A VersaModule Eurocard (VME) PC (VMIC 7751) with a Pentium III 733-MHz processor and 256 MB RAM is used. Several commercial software packages to control the 6-DOF maglev positioner were used, including Swiftnet (by Pentek), Code Composer (by Texas Instruments), and Visual C++ (by Microsoft). The Swiftnet acts as a control communication panel and mediates the data interaction between the VME PC and the DSP board. This software runs whenever the DSP is operational. The code composer compiles the source codes and generates the executable file to be run on the DSP.

2.4 Specifications of the precision positioner

Specifications of the positioner and the parameters of the magnet arrays and windings are presented in Tables 1 and 2, respectively. Table 3 shows the motion capabilities of the maglev positioner.

3 DYNAMIC MODELLING

3.1 Dynamic analysis

The total mass of the platen is $M = 5.91$ kg, so its weight is 57.98 N, which is made up of the Derlin triangular frame, three planar-motor windings, two stick mirrors, three vertical sensors with mounts, and the like. The three planar motors can generate a force of 68.60 N for vertical motion and thus the positioner can be levitated solely using the magnetic

(a)

(b)

(c)
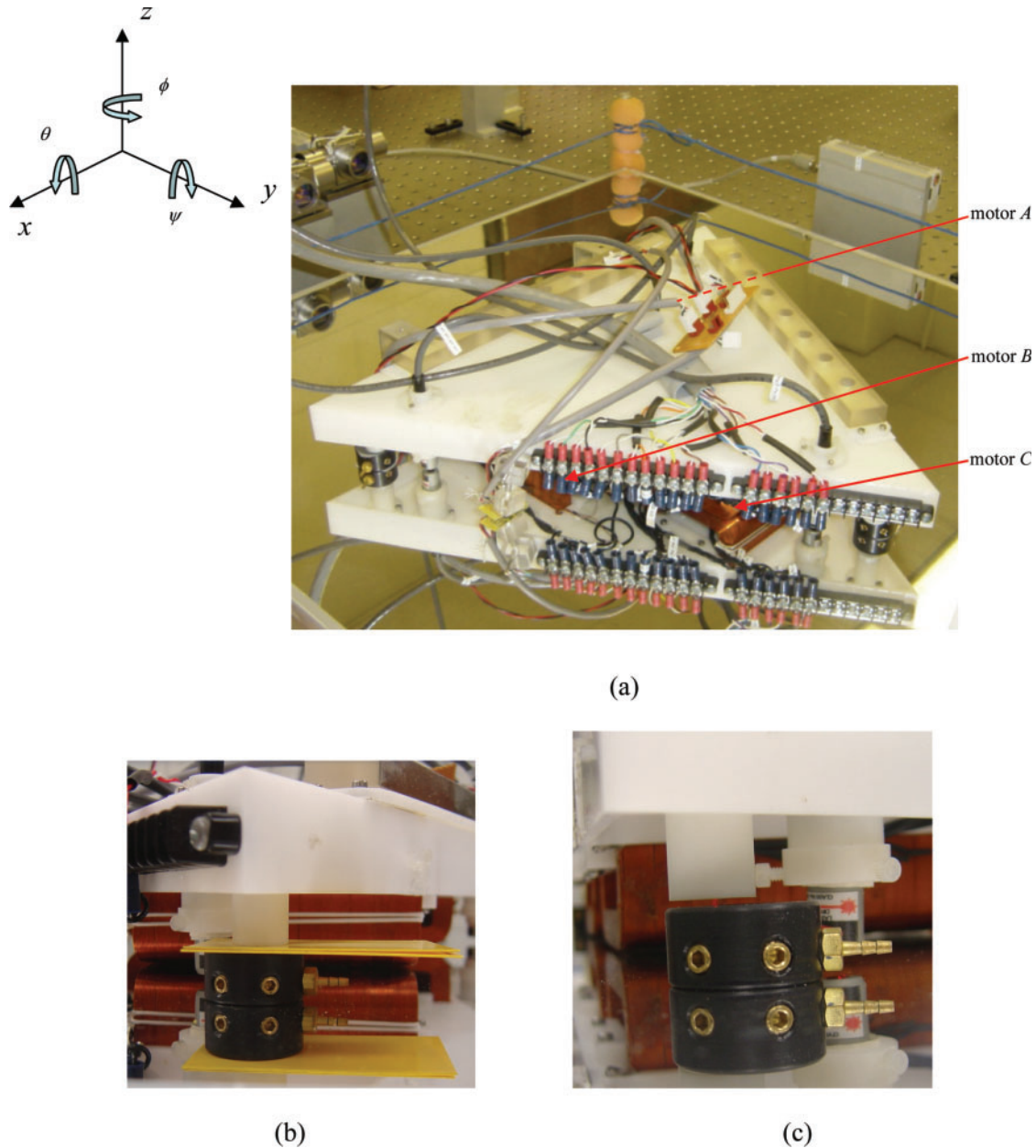
Fig. 3   (a) A photograph of the 6-DOF maglev positioner with high precision. The triangular platen is placed on top of a mirror-finished aluminium plate. Beneath the aluminium plate is the concentrated-field magnet matrix. (b) Initial setting with two 0.04-inch-thick shims, and (c) under magnetic levitation without shims

force. Table 2 lists the key parameters of the platen. The driving force of 22.87 N can be generated at a peak current density of $2 \times 10^6 \, \text{A/m}^2$. The whole system was designed using the Solidworks Program. The moments of inertia are calculated by Solidworks with respect to the centre of mass of the platen. The calculated mass centre and the moments of inertia are

$$CM = \begin{bmatrix} CM_x & CM_y & CM_z \end{bmatrix}^{\mathrm{T}}$$
$$= \begin{bmatrix} 191.8 & 106.6 & -1.0 \end{bmatrix}^{\mathrm{T}} \tag{1}$$

in units of millimetres. The inertia matrix of the platen is

$$\mathbf{I} = \begin{bmatrix} I_{xx} & -I_{xy} & -I_{xz} \\ -I_{yx} & I_{yy} & -I_{yz} \\ -I_{zx} & -I_{zy} & I_{zz} \end{bmatrix}$$
$$= \begin{bmatrix} 0.0357 & -0.00120 & -0.000808 \\ -0.00120 & 0.0261 & 0.000263 \\ -0.000808 & 0.000263 & 0.0561 \end{bmatrix} \tag{2}$$
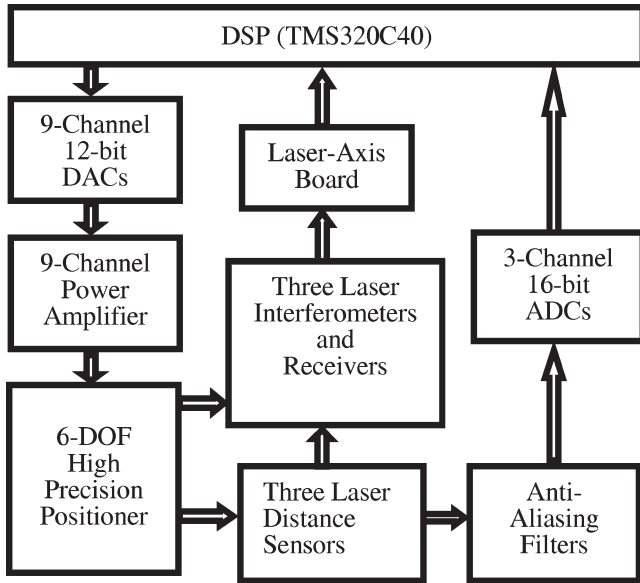
Fig. 4 Schematic diagram of the control structure

in units of kilogrammes metre squared. Products of the inertia, I_{xy}, I_{xz}, I_{yx}, I_{yz}, I_{zx}, and I_{zy} are neglected in the dynamic model, because their values are less than 5 per cent of the principal moments of inertia [**1**, **2**].

3.2 Linearized force equations

The planar motors are operated by the Lorentz-force law

$$F = J \times B \tag{3}$$

Specifically the following equation governs the orthogonal force components generated by one pitch of the levitation motor [**7**]

$$\begin{bmatrix} f_y \\ f_z \end{bmatrix} = \frac{1}{2} \mu_0 M_0 \eta_0 N_m G e^{-\gamma_1 z_0} \begin{bmatrix} \cos\gamma_1 y_0 & \sin\gamma_1 y_0 \\ -\sin\gamma_1 y_0 & \cos\gamma_1 y_0 \end{bmatrix} \begin{bmatrix} i_a \\ i_b \end{bmatrix} \tag{4}$$

where the f_y and f_z are y-directed and z-directed forces, respectively. Forces between the lateral and vertical motions are decoupled by a *DQ* decomposition so that we can control these two motions independently, which is discussed in the following section. The constant G is defined as

$$G = \frac{\sqrt{2} w l^2}{\pi^2} \left(1 - e^{-\gamma_1 \Gamma}\right) \left(1 - e^{-\gamma_1 \Delta}\right) \tag{5}$$

which has a value of $1.072 \times 10^{-5} \, \text{m}^3$. Here i_a and i_b represent the two-phase peak current components, and y_0 is the horizontal relative displacement of the motors A and B from the initial position. The absolute value of the fundamental wave number is

Table 1 Specifications of the positioner

Specification	Value
Number of phases	$q = 3$
Phase inductance (mH)	15.264
Phase resistance (Ω)	19.44
Nominal phase current (A)	0.56
Maximum phase current (A)	1.26
Nominal phase voltage (V)	11.6
Maximum phase voltage (V)	26.1
Moment arms (mm)	$l_{Ax} = 49.7$, $l_{Bx} = 52.7$ $l_{Cx} = 1.3$, $l_{Ay} = 44.8$ $l_{By} = 44.8$, $l_{Cy} = 84.3$

Table 2 Parameters of the magnet arrays and windings

Specification	Value
Turn density, η_0 (turns/m^2)	3.5246×10^6
Pitch, l (mm)	50.977
Magnet array width, w (mm)	12.7
Nominal motor air gap (mm)	2.324
Magnet matrix size (mm)	304.8×304.8
Number of magnet pitches, N_m	2
Magnet thickness, Δ	$l/4$
Winding thickness, Γ	$l/5$
Magnet remanence (T)	$B_r = \mu_0 M_0 = 0.71$
Nominal peak current density (A/m^2)	$J_p = 2 \times 10^6$

Table 3 The motion capabilities of the maglev positioner

Specification	Value
Planar travel range (mm)	120×120
Position resolution (nm)	20
Position noise (nm rms)	10
Angular resolution	Sub-microradian order
Nominal motor air gap (mm)	2.3
Vertical range (μm)	100
Maximum velocity (mm/s)	24.8

$\gamma_1 = 2\pi/l = 123.251/\text{m}$, $w = 12.7\,\text{mm}$ is the width of one magnet array, and $l = 50.977\,\text{mm}$ is the single actuator pitch. Δ, Γ, and z_0 denote the thickness of the magnet array, the thickness of the winding, and the nominal motor air gap, respectively. All key parameters are presented in Table 2.

3.3 *DQ* decomposition

The *DQ* decomposition methodology is used, to remove the sinusoidal non-linearity in equation (4) [**19**]. Both the direct-axis (*D*-axis) and the quadrature-axis (*Q*-axis) are attached to the mover so that the two axes move together with the platen as indicated in Fig. 5. Therefore there is no horizontal-position dependence in the force equations with respect to the stator so that the non-linear term can
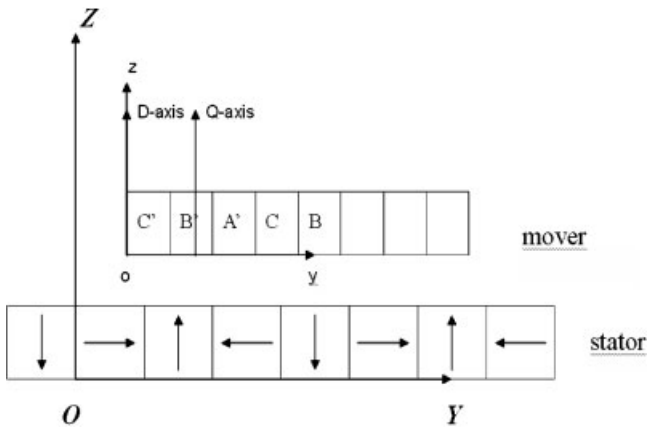
Fig. 5 *DQ* coordinates attached to the mover, or the platen [1–2]

be eliminated. The vertical motion is generated by the *D*-component current, and the horizontal motion by the *Q*-component current. In order to control the 2-DOF suspension and the driving forces independently, the planar motor generates decoupled two (*D*-axis and *Q*-axis) orthogonal force components. In the following sections linearized equations of motion are developed with this *DQ* decomposition theory.

3.4 Vertical equations of motion

The vertical equation of motion is represented as follows after *DQ* decomposition is applied

$$f_z - Mg =$$

$$3 \times \frac{1}{2} \mu_0 M_0 \eta_0 N_{\mathrm{m}} G \left(\mathrm{e}^{-\gamma_1 z_0} i_D - \gamma_1 \mathrm{e}^{-\gamma_1 z_0} i_D z_0 + \mathrm{e}^{-\gamma_1 z_0} i_D \right) \ (6)$$

The factor of three is a result of the point that all three planar motors contribute to the vertical force equally. Equation (7) is derived after cancelling the weight *Mg* with $3 \times \mu_0 M_0 \eta_0 N_{\mathrm{m}} G \mathrm{e}^{-\gamma_1 z_0} i_D / 2$, which is an equilibrium condition. Thus, the expression for the linearized vertical force with fixed z_0 is

$$f_z = 3 \times \frac{1}{2} \mu_0 M_0 \eta_0 N_{\mathrm{m}} G \mathrm{e}^{-\gamma_1 z_0} i_D$$

$$- 3 \times \frac{1}{2} \mu_0 M_0 \eta_0 N_{\mathrm{m}} G \gamma_1 \mathrm{e}^{-\gamma_1 z_0} i_D z_0 \qquad (7)$$

and the linearized incremental vertical equation of motion is thus

$$M \frac{\mathrm{d}^2 z_0}{\mathrm{d}t^2} + \mu_0 M_0 \eta_0 N_{\mathrm{m}} G \mathrm{e}^{-\gamma_1 z_0} i_D z_0$$

$$= 3 \times \frac{1}{2} \mu_0 M_0 \eta_0 N_{\mathrm{m}} G \gamma_1 \mathrm{e}^{-\gamma_1 z_0} i_D \qquad (8)$$

Likewise the linearized incremental lateral equation of motion can be derived as follows [20]

$$M \frac{\mathrm{d}^2 x_0}{\mathrm{d}t^2} - \mu_0 M_0 \eta_0 N_{\mathrm{m}} G \mathrm{e}^{-\gamma_1 z_0} i_D x_0$$

$$= \frac{1}{2} \mu_0 M_0 \eta_0 N_{\mathrm{m}} G \gamma_1 \mathrm{e}^{-\gamma_1 z_0} i_Q \qquad (9)$$

3.5 Force allocation for 6-DOF motion generation

Any 6-DOF motion can be generated by combination of the six independent force components generated by the three levitation motors, A, B, and C designated in Fig. 3(a). The *x*-axis motion is generated by motor C, and the other motors A and B cancel the torque. The *y*-axis motion is generated by motors A and C, and ϕ denotes the rotation about the *z*-axis contributed by all three motors. The vertical translation in *z* is generated by all three motors in the same vertical direction upward or downward, θ is the rotation about the *x*-axis, and ψ is the rotation about the *y*-axis, respectively.

The vertical dynamic equations are represented as a spring–mass system to accommodate the magnetic springs in the three levitation motors

$$M \frac{\mathrm{d}^2 \{z, \theta, \psi\}}{\mathrm{d}t^2} = f_{\{z, \theta, \psi\}} - K_{\{z, \theta, \psi\}} \{z, \theta, \psi\} \qquad (10)$$

$$f_z = f_{\mathrm{A}z} + f_{\mathrm{B}z} + f_{\mathrm{C}z} \qquad (11)$$

where f_z is the vertical directional force, generated by the three motors simultaneously in order to lift the platen up against gravity. Forces generated by the coils A, B, and C are denoted by f_{A}, f_{B}, and f_{C}, respectively

$$\tau_\theta = -f_{\mathrm{A}z} l_{\mathrm{A}y} - f_{\mathrm{B}z} l_{\mathrm{B}y} + f_{\mathrm{C}z} l_{\mathrm{C}y} \qquad (12)$$

$$\tau_\varphi = -f_{\mathrm{A}z} l_{\mathrm{A}x} - f_{\mathrm{B}z} l_{\mathrm{B}x} + f_{\mathrm{C}z} l_{\mathrm{C}x} \qquad (13)$$

where τ_θ and τ_ψ are the torques about the *x*- and *y*-axes, respectively, and $l_{\mathrm{A}y}$, $l_{\mathrm{B}y}$, $l_{\mathrm{C}y}$, $l_{\mathrm{A}x}$, $l_{\mathrm{B}x}$, and $l_{\mathrm{C}x}$ are the corresponding moment arms for motors A, B, and C. K_z is the effective spring constant of the levitation motor based on Hooke's law. K_θ and K_ψ are the effective torsional spring constants about the *x*- and *y*-axes. Their experimentally determined values are $K_z = 2382 \, \mathrm{N/m}$, $K_\theta = 7505 \, \mathrm{N/rad}$, and $K_\psi = 8319 \, \mathrm{N/rad}$, respectively. The linearized lateral equation of motion, equation (9), is further simplified, and the platen is modelled as a pure mass without friction in full levitation. The following equations represent the lateral dynamics of the pure mass model

$$M\frac{d^2\{x,y,z\}}{dt^2}=f_{\{x,y,z\}} \qquad (14)$$

$$f_x=f_{Cx} \qquad (15)$$

where the mass of platen is $M = 5.91$ kg, and f_x is the magnetic modal force generated by motor C. In the y-axis

$$f_y=f_{Ay}+f_{By} \qquad (16)$$

where f_y is the y-direction magnetic modal force generated by motors A and B.

In ϕ

$$\tau=-f_{Ax}l_{Ay}+f_{By}l_{Bx}-f_{Cx}l_{Cy} \qquad (17)$$

where l_{Ay}, l_{Bx}, and l_{Cy} are the corresponding moment arms for motors A, B, and C, respectively.

The weight of the platen is 57.98 N. As can be seen in Table 1, the nominal phase current is 0.56 A and the phase resistance is 19.44 Ω. Therefore, the dissipated power by each phase on average would be

$$Power=i_{A1}^2 \times R=(0.56)^2(19.44)=6.0964 \text{ W} \qquad (18)$$

Each motor consists of three phases, and three planar motors generate all 6-DOF motions together so that the total power dissipation is $9 \times Power = 54.8675$ W. As a result, a force-generation versus power dissipation number would be 54.8675/57.98 = 0.946 W/N.

4 CONTROLLER DESIGN

4.1 Controller for the vertical mode

With the parameter values given in the previous section, the decoupled vertical dynamic equation of motion is

$$M\frac{d^2z}{dt^2}+2\mu_0 M_0\eta_0 N_m G\gamma_1 e^{-\gamma_1 z}i_D z$$
$$=2\mu_0 M_0\eta_0 N_m Ge^{-\gamma_1 z}i_D \qquad (19)$$

$$5.91\frac{d^2z}{dt^2}+2382z=f_z \qquad (20)$$

where f_z is the modal force and is the sum of the decomposed vertical force, and the magnetic spring constant of $K = 2382$ N/m was obtained by experiment. The following lead-lag compensator with the damping ratio $\zeta = 0.5$ was designed with the MATLAB single-input single-output (SISO) tools

$$G_z(s)=2300\,642 \times \left(\frac{s+137.21}{s+1036}\right)\left(\frac{s+10}{s}\right) \qquad (21)$$

The closed-loop dominant poles are located at $-289 \pm j192$ rad/s, and the phase margin (PM) is 50° at the cross over frequency of 55 Hz. Then, using the pole-zero mapping technique, the controller is transferred to the digital lead-lag compensator as follows

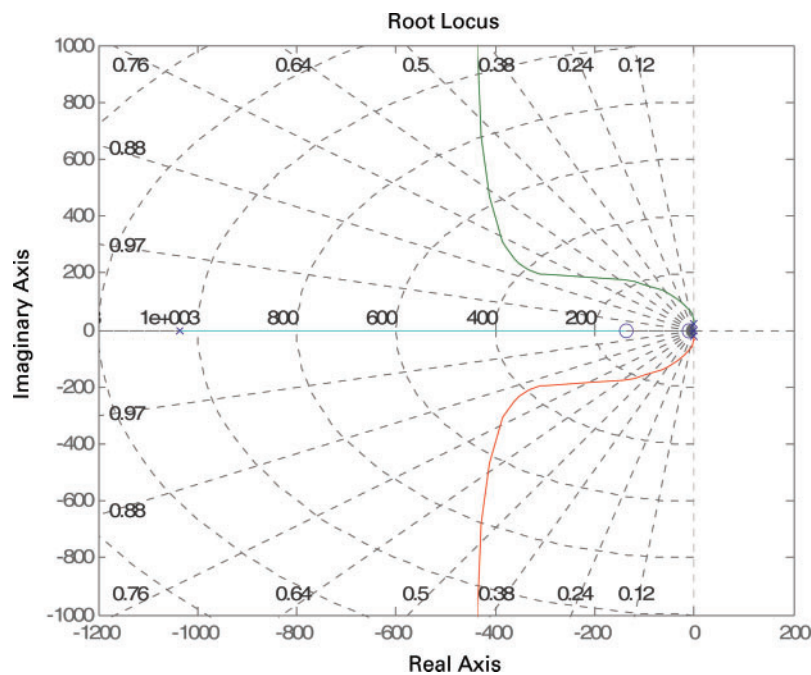$$G_z(z)=2126\,342 \times \left(\frac{z-0.9754}{z-0.8129}\right)\left(\frac{z-0.998}{z-1}\right) \qquad (22)$$

Fig. 6 Root locus for z

Figure 6 represents the root locus for dominant poles. The cross symbols (×) denote the chosen closed-loop poles. The Bode plots of the loop transfer function with a resonance peak at 3.18 Hz and the closed-loop transfer function for z are shown in Fig. 7.

The controller for the vertical degree-of-freedom in θ was designed after the control loop for z was closed. A moment of inertia of $I_{xx} = 0.0357$ kg-m^2 is used with respect to the geometrical symmetry of the platen

$$G_\theta(s) = 5703 \times \left(\frac{s+91.47}{s+690.5}\right)\left(\frac{s+10}{s}\right) \qquad (23)$$

The closed-loop dominant poles are located at $-185 \pm j130$ rad/s, and the PM is 50° at the crossover frequency of 35 Hz. The converted digital controller in θ is

(a)

(b)
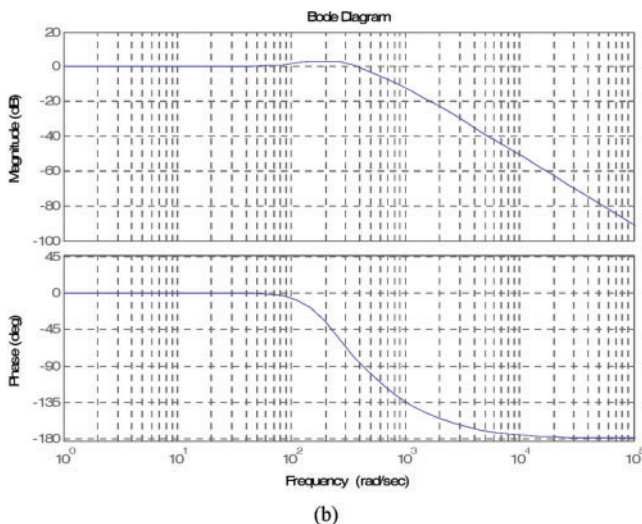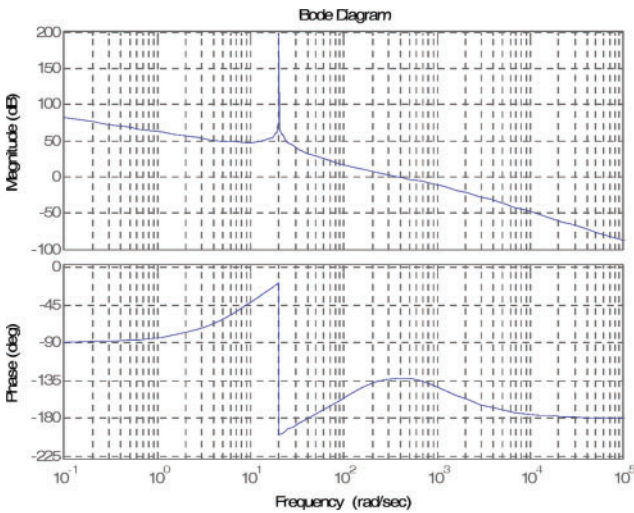
Fig. 7 (a) Loop transfer function and (b) closed-loop Bode plot, for z

$$G_\theta(z) = 5431 \times \left(\frac{z-0.983}{z-0.871}\right)\left(\frac{z-0.998}{z-1}\right) \qquad (24)$$

Another controller in ψ was also designed with the same method with a different moment of inertia ($I_{yy} = 0.0261$ kg-m^2). It has the same structure as equation (24) but has a control gain of 4321 N/rad. The dominant poles are located at $-185 \pm j130$ rad/s and the PM is 50° at the crossover frequency of 36 Hz.

4.2 Controller for the lateral mode

After the geometric parameters were substituted, the decoupled lateral dynamic equation of motion, equation (14), becomes

$$5.91 \frac{\mathrm{d}^2 x}{\mathrm{d}t^2} = f_x \qquad (25)$$

where f_x is a modal force and is the sum of the decomposed lateral force components. The following lead-lag compensator for x and y was designed using MATLAB SISO tools

$$G_{x,y}(s) = 9.0 \times 10^5 \times \left(\frac{s+55.6904}{s+1134.2247}\right)\left(\frac{s+10}{s}\right) \qquad (26)$$

The PM is 58° at the crossover frequency of 21 Hz. The controller for ϕ has the same structure as equation (26) with a controller gain of 1.5×10^4 N/rad. The PM is 63° at the crossover frequency of 38 Hz. All compensators have a sampling frequency of 5 kHz.

5 CLOSED-LOOP EXPERIMENTAL RESULTS

5.1 Experimental set-up

All 6-DOF motions were tested after the real-time controllers designed in section 4 had been implemented. This research uses pure magnetic force to levitate the platen against gravity, successfully eliminating the aerostatic bearings employed in the previous work reported in [1]. Figures 3(b) and 3(c) are photographs of the initial position setting before and after the maglev principle was applied. Nanoscale positioning resolution, fast response, and large trajectories are required in semiconductor engineering applications [21].
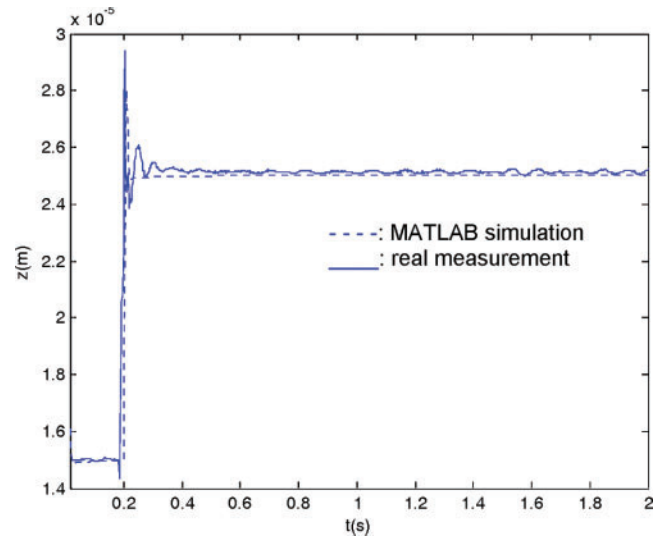
5.2 Step responses

Simulated step responses obtained by using MATLAB and experimental step responses in the x- and y-axes are shown in Fig. 8. Figure 9 also presents

(a)

(b)
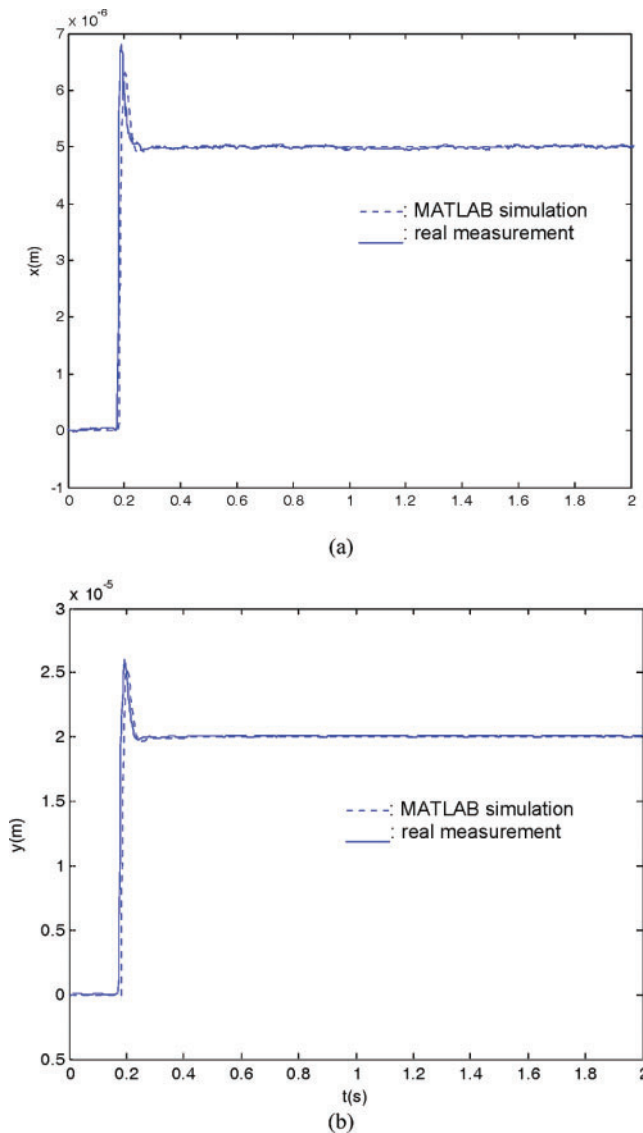
Fig. 8 Step responses by MATLAB simulation (dashed) and experiments (solid). (a) 5 μm in x and (b) 20 μm in y

closed-loop step responses in z generated by MATLAB simulation (dashed lines) and obtained by experiments (solid lines), which match very well. These plots show that the rise time is less than 3 ms, the settling time is around 100 ms without any steady state error, and the overshoot is about 20 per cent. The initial position of z was set at 1.5 μm, and a 10 μm step command was given to the system. Three vertical laser distance sensors (Nanogage 100) with a 15 nm position resolution are used in these studies. These analogue sensors generate more noise in vertical motions than in lateral motions in x and y. A fluctuation in the initial position just before the step command might have generated the dip in the step response. The authors doubt that this originated

Fig. 9 10 μm step response in z by real measurement (solid) and MATLAB simulation (dashed)

from any non-minimum-phase zero in the system. Small oscillations occurred, especially in z, due to the disturbance transmitted through the laboratory floor and the dynamics of the power cables connected to the VME chassis even though a vibration-isolation optical table (Newport RS 3000) was used in these experiments. Figure 9 exhibits about a 0.1 μm steady state position error between the simulation and the real measurement response. This was probably caused by misaligned vertical position sensors or external disturbances.

Figure 10 shows the maglev stage's capability in nanoscale stepping motion in x. Figure 10(a) is a 50 nm step response in x, and Fig. 10(b) is its fast-Fourier-transform (FFT) plots. There is a 10-nm root mean square position noise with the dominant noise frequency occurring at approximately 150 Hz.

5.3 Long-range scanning motion

Long-range scanning motion is common in precision applications such as microlithography. Several experimental results to demonstrate the two-dimensional and three-dimensional scanning capabilities of this 6-DOF maglev positioner are presented in this section.

Figure 11(a) shows a 5-mm radius planar circular trajectory and Fig. 11(b) a star-shaped trajectory traversed by the positioner. The angular velocity was 0.5 rad/s for the circlular case, and the linear velocity was 2.5 mm/s for the star-shape motion. Figure 12 demonstrates the 120×120 mm maximum travel range of the 6-DOF maglev positioner. The linear scanning velocity was 2.48 mm/s in both the x- and y-
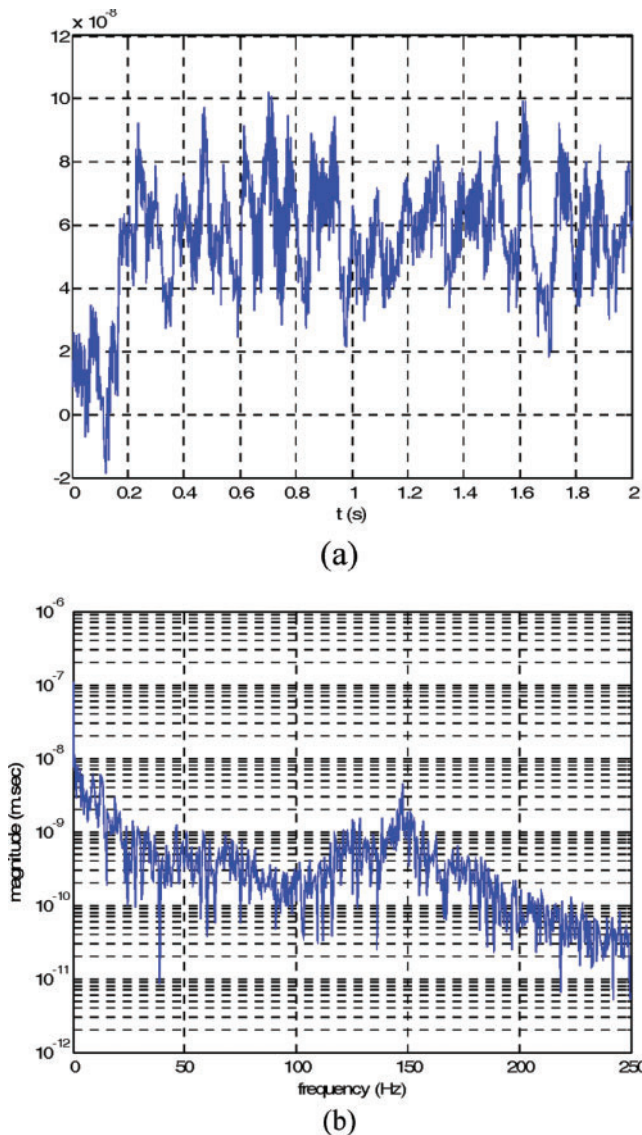
Fig. 10 (a) 50 nm step response in x and (b) its FFT

directions. Outside of this planar range the positioner would lose the laser beams for the planar-position measurement and become unstable at the corners.

Figure 13 shows a 1 µm amplitude sinusoidal motion in y. This result highlights that the positioner has the capability of microscale one-dimensional and two-dimensional motion. This precision positioner can also move in the z-direction within the laser sensor's distance range of 100 µm. Figure 14 shows a three-dimensional spring-shaped motion generated by the positioner. It represents seven circles of a 500 µm radius with a 2.3 rad/s angular velocity. The maximum velocity of 24.8 mm/s is presented in Fig. 15. This is the part of back-and-forth motions with a 10 mm step size in the y-direction.
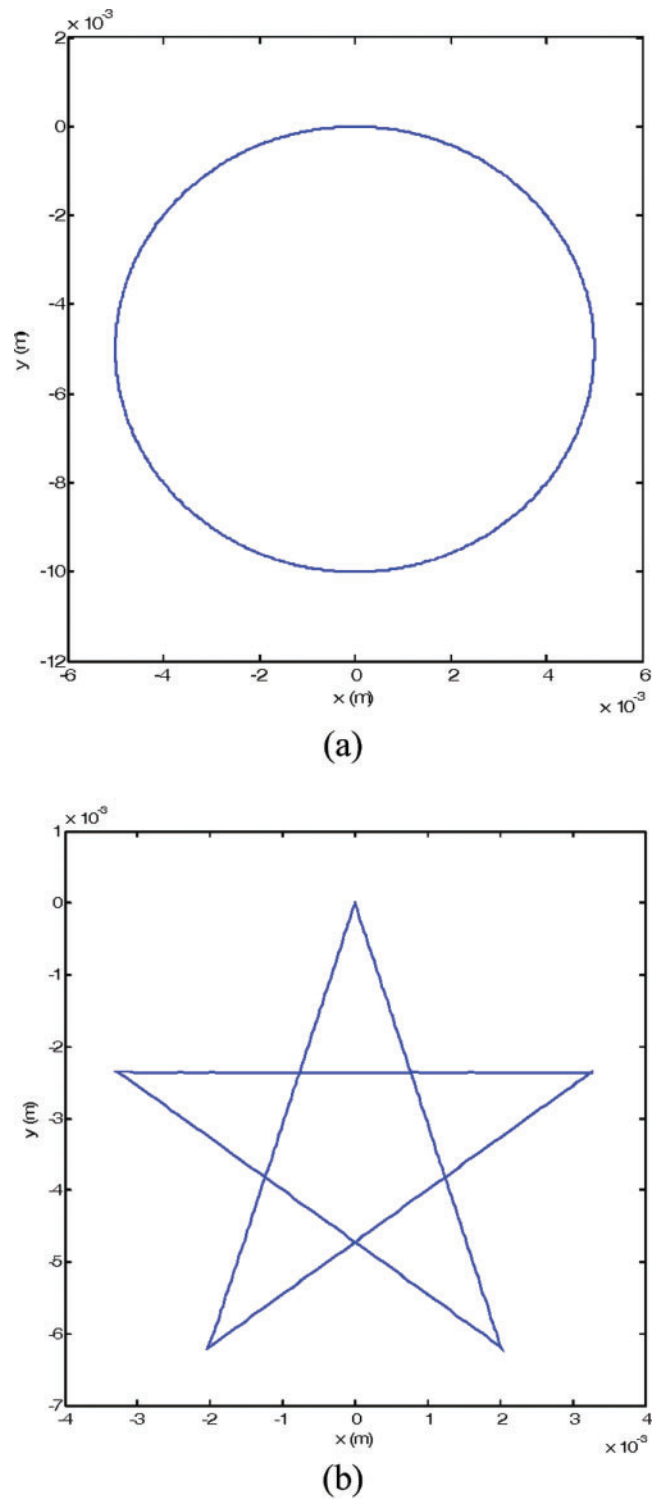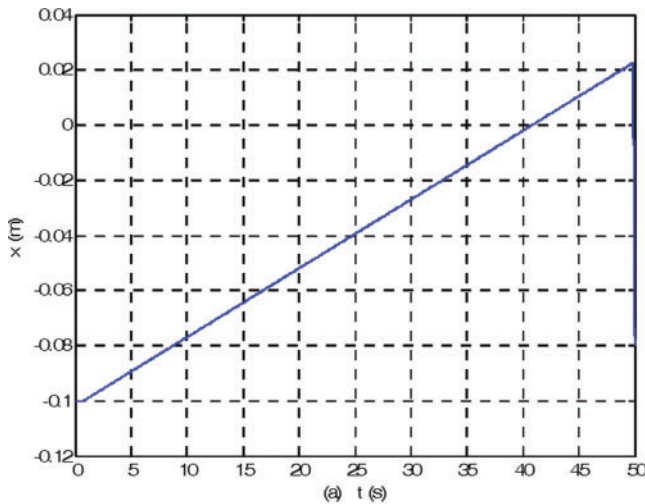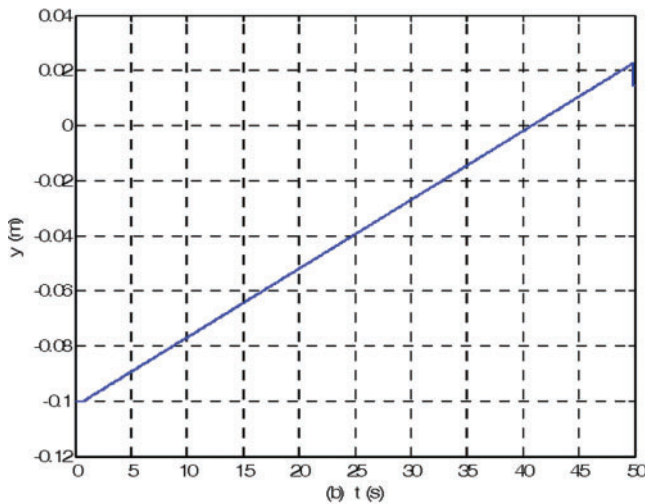

Fig. 11 Capability of following paths with (a) a 5 mm radius circular motion, and (b) a star-shaped motion

6 CONCLUSIONS

The 6-DOF high-precision maglev positioner consists of a single triangular moving platen with a 5.91 kg

(a)

(b)
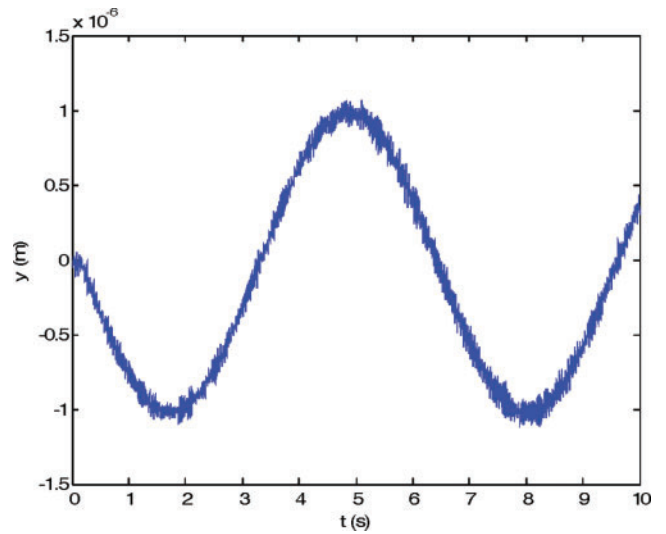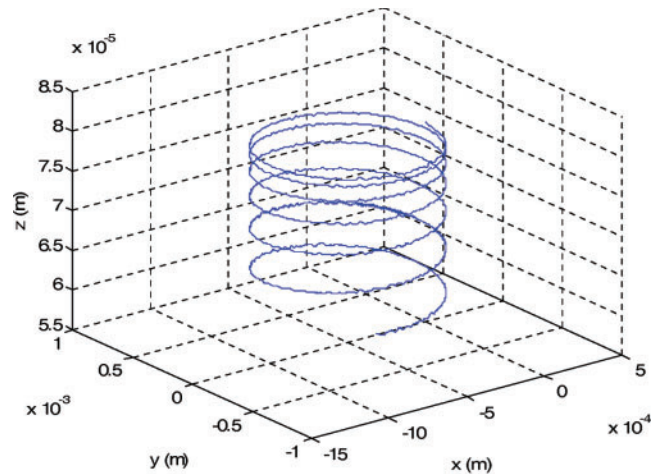
Fig. 12 120 mm maximum travel range in (a) x and (b) y

Fig. 13 1 μm amplitude sinusoidal motion in y

Fig. 14 500 μm radius three-dimensional spring-shaped trajectory

mass, a novel concentrated-field magnet matrix with dimensions $304.8 \times 304.8 \times 12.7$ mm, and three planar motors generating all six-axis motions. The single moving platen can generate all six-axis fine and coarse motions with magnetic force alone. Furthermore, the maglev stage requires no lubricant and produces no wear particles since there are no mechanical contacts, so it can be used in clean-room environments. Because this precision positioner has a simple mechanical structure in a single-moving frame, its fabrication cost is not as high as that of other currently available positioning systems.

The paper presents the real-time digital controller design and implementation and several key experimental results with the 6-DOF high-precision ma-

glev positioner. The aerostatic bearings used in previous work were removed successfully, and all 6-DOF motions are controlled solely by the application of the magnetic force. The sampling rate of the control system was 5 kHz.

Position resolution of 20 nm with a position error of 10 nm root mean square was achieved. The experimentally demonstrated maximum travel range is 120×120 mm. The positioner exhibits a 24.8 mm/s maximum velocity. Step responses of 5 μm, 10 μm, and 20 μm in the x, y, and z directions were provided, and 5 mm radius circular, star-shaped translational, micro-scale sinusoidal, and 500-μm-radius spring-shaped three-dimensional motions were also presented. The utility of the high-precision maglev stage for nano- and microscale positioning was successfully demonstrated.
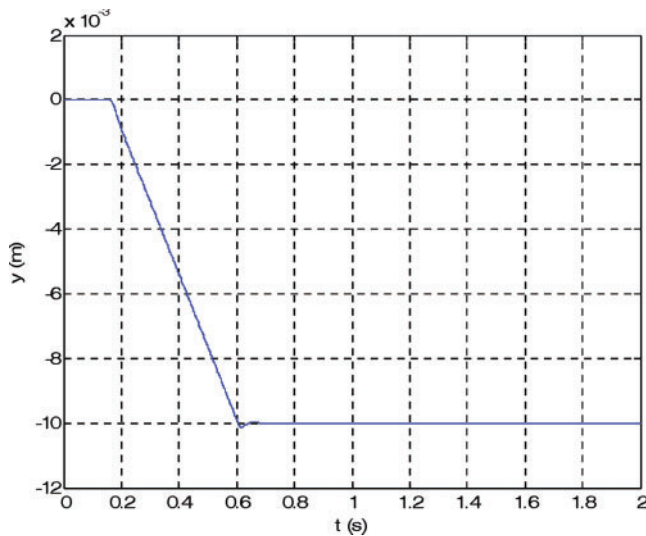
Fig. 15 Velocity profiles in *y* with a 24.8 mm/s maximum velocity

ACKNOWLEDGEMENTS

REFERENCES

1 **Hu, T.** *Design and control of a 6-degree-of-freedom levitated positioner with high precision.* PhD Thesis, Department of Mechanical Engineering, Texas A&M University, College Station, Texas, May 2005.
2 **Hu, T.** and **Kim, W.-J.** Extended-range 6-DOF high-precision positioner for wafer processing. *IEEE/ASME Trans. Mechatronics*, 2006, **11**(6), 682–689.
3 **van Engelen, G.** and **Bouwer, A. G.** *Two-step positioning device using Lorentz forces and a static gas bearing*, 1992, US patent number 5120034.
4 **Sakino, S., Osanai, E., Negishi, M., Horikoshi, M., Inoue, M.,** and **Ono, K.** *Movement guiding mechanism*, 1999, US patent number 5040431.
5 **Wittekoek, S.** and **Bouwer, A. G.** *Displacement device, particularly for the photolithographic treament of a substrate*, 1987, US patent number 4655594.
6 **Salapaka, S.** and **Sebastian, A.** Design of high precision high bandwidth and reliable nanopositioning systems. In Proceedings of *2003* ASME International Mechanical Engineering Congress and Exposition, November 2003, paper 55554 (ASME, New York, NY, USA).
7 **Xu, Z., Feng, Z., Seto, K.,** and **Tamura, H.** Nonlinear vibration properties of a current-controlled attractive type maglev system. In Proceedings of 2003 ASME International Mechanical Engineering Congress and Exposition, November 2003, paper 41879 (ASME, New York, NY, USA).
8 **Hinds, W. E.** and **Nocito, B.** The Sawyer linear motor. In Proceedings of the Second Symposium on *Incremental motion control systems and devices*, Urbana, Illinois, 1973, pp. W-1–W-10 (University of Illinois, Urbana, USA).
9 **Asakawa, T.** *Two dimensional positioning devices*, 1986, US patent number 4626749.
10 **Asakawa, T.** *Two dimensional precise positioning devices for use in a semiconductor apparatus*, 1985, US patent number 4535278.
11 **Pelta, E. R.** Two axis Sawyer motor for motion systems. *IEEE Control Syst. Mag.*, 1987, **7**, 20–24.
12 **Fujii, N.** and **Kihara, T.** Surface induction motor for two-dimensional drive. *J. Inst. Elect. Engng Trans.*, 1998, **4**, 221–228.
13 **Chitayat, A.** *Two-axis motor with high density magnetic platen*, 1998, US patent number 5777402.
14 **Pelta, E. R.** Two axis Sawyer motor. In Proceedings of the 12th Annual IEEE Industrial Electronics Society Conference, Urbana, Illinois, 1986, pp. 3–8 (IEEE, Piscataway, NJ, USA).
15 **Compter, Ir. J. C.** Electro-dynamic planar motor. *Precision Engng*, 2004, **28**, 171–180.
16 Normag, *Northern magnetics linear motor technology Manual*, 1998 (Baldor, Fort Smith, AR, USA).
17 Megamation. http://www.megamation.com/hm_frame.htm, 2001.
18 **Trumper, D. L., Kim, W.-J.,** and **Williams, M. E.** *Magnetic arrays*, 1997, US patent number 5631618.
19 **Kim, W.-J.** *High-precision planar magnetic levitation*. PhD Thesis, Department of Electrical Engineering and Computer Science, Massachusetts Institute of Technology, 1997.
20 **Kim, W.-J., Bhat, N.,** and **Hu, T.** Integrated multi-dimensional positioner for precision manufacturing. *J. Engng Mf.*, 2004, **218**(4), 431–442.
21 **Quirk, M.** and **Serda, J.** *Semiconductor manufacturing technology*, 2001 (Prentice-Hall, NJ, USA).